

Contribution of a Disk Component to Single Peaked Broad Lines of Active Galactic Nuclei

E. Bon^{1,2}, L. Č. Popović^{1,2}, N. Gavrilović^{1,2,3}, G. La Mura⁴, E. Mediavilla⁵

¹*Astronomical Observatory, Volgina 7, 11160 Belgrade 74, Serbia, email: ebon@aob.bg.ac.yu*

²*Isaac Newton Institute of Chile, Yugoslavia Branch*

³*Observatoire de Lyon, 9 Avenue Charles André, Saint-Genis Laval Cedex, F-69561, France*

⁴*Department of Astronomy, University of Padova, Vicolo dell'Osservatorio, I-35122 Padova, Italy*

⁵*Instituto de Astrofísica de Canarias, Tenerife, Spain*

Accepted 1988 December 15. Received 1988 December 14; in original form 1988 October 11

ABSTRACT

We study the disk emission component hidden in the single-peaked Broad Emission Lines (BELs) of Active Galactic Nuclei (AGN). We compare the observed broad lines from a sample of 90 Seyfert 1 spectra taken from the Sloan Digital Sky Survey with simulated line profiles. We consider a two-component Broad Line Region (BLR) model where an accretion disk and a surrounding non-disk region with isotropic cloud velocities generate the simulated BEL profiles. The analysis is mainly based in measurements of the full widths (at 10%, 20% and 30% of the maximum intensity) and of the asymmetries of the line profiles. Comparing these parameters for the simulated and observed H α broad lines, we found that the hidden disk emission may be present in BELs even if the characteristic of two peaked line profiles is absent. For the available sample of objects (Seyfert 1 galaxies with single-peaked BELs), our study indicates that, in the case of the hidden disk emission in single peaked broad line profiles, the disk inclination tends to be small (mostly $i < 25^\circ$) and that the contribution of the disk emission to the total flux should be smaller than the contribution of the surrounding region.

Key words:

galaxies: Seyfert, accretion, accretion disks, line: profiles.

1 INTRODUCTION

Modeling of the double-peaked Balmer lines has been used to study the emission gas kinematics of the Broad Line Region (BLR) (see e.g. Perez et al. 1988; Chen et al. 1989; Chen & Halpern 1989; Eracleous & Halpern 1994, 2003; Rodríguez-Ardila et al. 1996; Storchi-Bergmann et al. 1997; Livio & Xu 1997; Ho et al. 2000; Shields et al. 2000; Strateva et al. 2003; Storchi-Bergmann et al. 2003a,b). However, only a small fraction of Active Galactic Nuclei – AGN (3%-5%) shows clearly double peaked Broad Emission Lines (BELs) in their spectra (Strateva et al. 2003).

According to the standard unification model (Urry & Padovani 1995) one can expect an accretion disk around a supermassive black hole in all AGN. The majority of AGN with BELs, have only single peaked lines, but this does not necessarily indicate that the contribution of the disk emission to the BELs profiles is negligible. It is well known that a face-on disk also emits single peaked broad lines (see e.g. Chen & Halpern 1989; Dumont & Collin-Souffrin 1990; Kollatschny & Bischoff

2002; Kollatschny 2003). Moreover, a Keplerian disk of arbitrary inclination with presence of a disk wind can also produce single-peaked broad emission lines (Murray & Chiang 1995).

In spite that most of the BELs are single peaked, there are other evidences like the detection of asymmetries and substructure (shoulders or bumps, for instance) in the line profiles that indicate the presence of a disk (or disk-like) emission (Popović et al. 2002; Kollatschny 2003; Shapovalova et al. 2004). Also, the study of the accretion rates in AGN supports the presence of a standard optically thick and geometrically thin disk (Wang et al. 2003). Moreover, the spectropolarimetric observations gave an evidence for the disk-like emission (rotational motion, see e.g. Smith et al. 2005)

To explain the complex morphology of the observed BELs shapes, different geometrical models have been discussed (see in more details Sulentic et al. 2000). In some cases the BELs profiles can be explained only if two or more kinematically different emission regions are considered (see

e.g. Romano et al. 1996; Popović et al. 2001, 2002, 2003, 2004, 2008, 2009; Bon et al. 2006; Bon 2008; Ilić et al. 2006; Collin et al. 2006; Hu et al. 2008). In particular, the existence of a Very Broad Line Region (VLBR) with random velocities at 5000-6000 km/s within an Intermediate Line Region (ILR) has also been considered to explain the observed BELs profiles (Corbin & Boroson 1996; Sulentic et al. 2000; Hu et al. 2008).

In this paper we study the presence of the hidden disk emission in objects which show only one dominant peak in their broad emission line profiles. To do that we consider that the BLR has two kinematic components; an accretion disk and a surrounding non-disk region. With this model we compute emission line profiles for different values of the model parameters. Then we compare the simulated profiles (specifically, their widths and asymmetries) with the observational data.

The aim of this paper is to discuss possibility that the disk geometry, at least partly, affects the complex BEL profiles, i.e. to try to constrain the BLR geometry that is important for estimates of the AGN black hole masses and accretion rates (see e.g. La Mura et al. 2009).

The paper is organized as follow: in §2 we describe the two component model of the BLR and perform the numerical simulation. In §3 we compare the simulations with available data. In §4 we discuss our results and in §5 we outline our conclusions.

2 NUMERICAL SIMULATIONS BASED ON A TWO-COMPONENT MODEL

2.1 BLR geometry

In the last years, arguments supporting the presence of disk winds show ability to explain a number of observed AGN phenomena such as the X-ray and UV absorption, line emission, reverberation results, some differences among Seyfert and other active objects (like quasars or broad-line radio galaxies), and the presence or absence of double-peaked emission-line profiles (see e.g. Murray & Chiang 1995, 1998; Proga & Kallman 2004). These results support a model in that the BLR is composed from two kinematically distinct components, a disk and a wind. Recently, Hu et al. (2008) confirmed that the BLR is probably composed from two emission regions, i.e. a VBLR and a ILR component, as it was earlier assumed in several papers (see e.g. Corbin & Boroson 1996; Sulentic et al. 2000; Popović et al. 2004, etc.).

Consequently, we assumed that the BELs can be kinematically divided into two components, one from the VBLR (contributing to the wings) and other from the ILR (contributing to the core). Of course, one can assume different geometries for both emitting regions (see e.g. Popović et al. 2004, and also Appendix B in this paper), but here we will assume that the VBLR is coming from an accretion disk, and the ILR from an additional region, which surrounds the disk, and has an isotropically distributed random velocity. Note here that the kinematics of a wind would imply radial velocities (logarithmic profile), more than isotropic (Gaussian profile), but we assume Gaussian profile as a first approximation. The scheme of the assumed model is presented in Fig. 1.

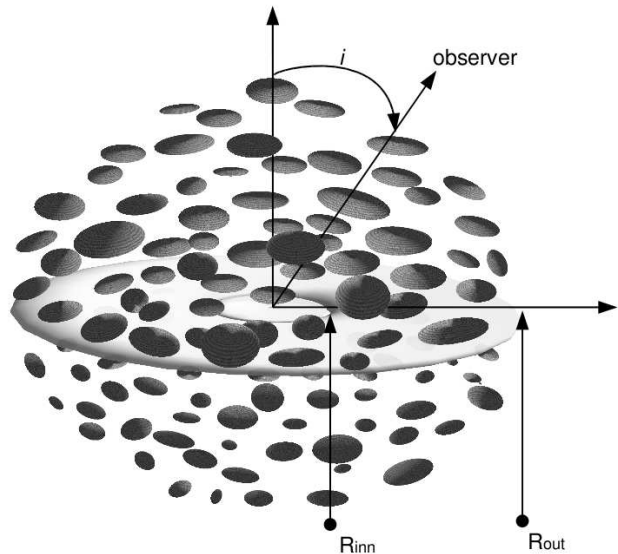


Figure 1. The scheme of the BLR composed from two geometrically different components: accretion disk and clouds randomly distributed around the disk.

The local broadening (σ) and shift (z_l) of each disk element have been taken into account as in Chen & Halpern (1989), i.e. the δ function has been replaced by a Gaussian function:

$$\delta \rightarrow \exp \frac{(\lambda - \lambda_0 - z_l)^2}{2\sigma^2}, \quad (1).$$

We express the disk dimension in gravitational radii ($R_g = GM/c^2$, G being the gravitational constant, M the mass of the central black hole, and c the velocity of light).

On the other hand, we assume that the additional emission region can be described by a surrounding region with an isotropic velocity distribution, i.e. the emission line profile generated by this region can be described by a Gaussian function with broadening w_s and shift z_s . Thus, the whole line profile can be described by the relation:

$$I(\lambda) = I_d(\lambda) + I_s(\lambda), \quad (2)$$

where $I_d(\lambda)$, and $I_s(\lambda)$ are the emissions of the relativistic accretion disk and the non-disk region, respectively.

2.2 Parameters for the disk and surrounding region

As it was earlier noted in Popović et al. (2004), this two component model can fit the line profiles of BELs, but is too open to constrain the physical parameters. First of all, the disk model includes many parameters (the size of the emitting region, the emissivity and inclination of the disk, the velocity dispersion of the emitters in the disk, etc.). Therefore, in order to do numerical tests, one needs to introduce some constraints and approximations.

It seems that the parameter σ of the Doppler broadening of the non-disk region and parameter σ corresponding to the broadening of the random motion in the disk model are connected (see Popović et al. 2004; Bon et al. 2006). As a

first approximation we assume that the random velocities in the disk and in the non-disk region are the same. So here we consider a parameter $\sigma = 1000$ km/s for both, the Doppler broadening of the non-disk regions as well as the σ in the model of the disk profile (also, see Eracleous & Halpern 2003)).¹

On the other hand, we considered a wide range of disk parameters but with several constraints:

i) The disk inclination affects the emission obtained from the disk. The observed flux from the disk (F_d) is proportional to the disk surface (S_d), as

$$F_d \sim S_{\text{eff}} \sim S_d \cdot \cos(i), \quad (3)$$

where i is the inclination, and S_{eff} is the effective disk emitting surface, therefore, one cannot expect a high contribution of the disk emission to the total line profile for a near edge-on projected disk.

ii) As far as the plasma inside 100 gravitational radii from the central black hole is very hot, one cannot expect emission of the low ionized lines in this part of the disk. Then we limit the inner radius to $R_{\text{inn}} > 100 R_g$. Consequently, the model given by Chen & Halpern (1989) can be properly used, i.e. it is not necessary to include a full relativistic calculation (as e. g. in Jovanović & Popović 2008).

iii) The emissivity of the disk as a function of radius, r , is given by $\epsilon = \epsilon_0 r^{-p}$. Since the illumination is due to a point source radiating isotropically, located at the center of the disk, the flux in the outer disk at different radii should vary as r^{-3} (Eracleous & Halpern 1994). We note here that this is indeed the way how the incident flux varies, but not necessarily the way in which lines respond to it (see e.g. Dumont & Collin-Souffrin 1990; Rokaki & Boisson 1999; Eracleous & Halpern 2003). However, the power index $p \approx 3$ can be adopted as a reasonable approximation at least for $H\alpha$ (Eracleous & Halpern 2003). Also, Cao & Wang (2006) indicate that p is in the range from 2 to 3. Moreover we simulated the influence of the emissivity (p) to the disk line profile (Fig. 2) and found that it only slightly affected the normalized disk line profiles. Therefore the assumption of $p = 3$ can be accepted for purposes of this work.

iv) Previous estimations of the double-peaked AGN emission lines (see e.g. Perez et al. 1988; Chen et al. 1989; Chen & Halpern 1989; Eracleous & Halpern 1994; Rodríguez-Ardila et al. 1996; Storchi-Bergmann et al. 1997; Ho et al. 2000; Shields et al. 2000; Strateva et al. 2003; Storchi-Bergmann et al. 2003a,b; Eracleous & Halpern 2003) show that the typical dimensions of an accretion disk that emits low ionization lines are of the order of several thousands R_g . For that reason we did not consider dimensions of the disk larger than 100000 R_g . This was an important approximation to limit the computing time.

v) We consider a systemic velocity shift of the non-disk region (not greater than ± 3000 km/s) to test the possibility of the outflow/inflow.

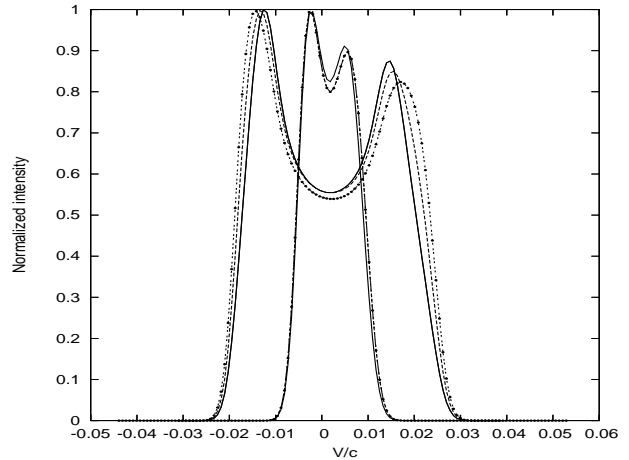


Figure 2. Simulated disk profiles for different values of the emissivity: $p=2$ (solid line) $p=3$ (dashed line) and $p=4$ (dotted-dashed line), for two inclinations $i = 10$ (narrower lines) and 30 degrees (broader line profiles). The inner and outer radius are taken as: $R_{\text{inn}} = 500 R_g$ and $R_{\text{out}} = 1500 R_g$. The maximum intensity is scaled to one.

2.3 Flux ratio, normalized widths and asymmetry parameters

We consider the following parameters to study the simulated and observed BELs profiles:

i) The flux ratio between the disk (F_d) and the non-disk region (F_s):

$$Q = \frac{F_s}{F_d} \quad (4),$$

where

$$F_{\text{tot}} = F_s + F_d = (1 + Q)F_d$$

Using this parameter, the total line profile (normalized to the disk flux)² can be written as:

$$\frac{I_{\text{tot}}(\lambda)}{F_d} = \frac{I_d(\lambda)}{F_d} + Q \frac{I_s(\lambda)}{F_s}, \quad (5)$$

where $I(\lambda)$ is the wavelength dependent intensity. The composite profile is normalized according to,

$$\mathfrak{S}(\lambda) = \frac{I_{\text{tot}}(\lambda)}{I_{\text{tot}}^{\text{max}}}, \quad (6)$$

where $I_{\text{tot}}^{\text{max}}$ is the maximum intensity of the composite line profile.

ii) For the composite line profile $\mathfrak{S}(\lambda)$ we measured full widths at 10%, 20%, 30% and 50% of the maximum intensity, i.e. $w_{10\%}$, $w_{20\%}$, $w_{30\%}$ and $w_{50\%}$. Then we define coefficients k_i ($i = 10, 20, 30$) normalized to the Full Width at Half Maximum (FWHM), as $k_{10} = w_{10\%}/w_{50\%}$, $k_{20} = w_{20\%}/w_{50\%}$ and $k_{30} = w_{30\%}/w_{50\%}$. It is obvious that the

¹ In Appendix A we give simulations of different σ for non-disk region

² This is taken from technical reasons to simulate different contributions of the disk and the non-disk component. First we normalized both line profiles to their fluxes, and after that we rescaled the non-disk component multiplying with Q , then whole profile is given in units of the disk flux.

coefficients k_i are functions of the radius R and other parameters of the disk. Using these normalized widths we can compare results from AGN with different random velocities.

iii) We also measured the asymmetry (A_i) at $i = 10\%$, 20% , 30% of maximum intensity of the modeled and observed lines as

$$A_i = \frac{W_i^R - W_i^B}{FWHM}, \quad (7)$$

where W_i^R and W_i^B are red and blue half widths at $i = 10\%$, 20% and 30% of the maximum intensity, respectively.

2.4 Simulated line profiles

First of all, we simulated only the disk profiles, taking into account different values of the disk parameters. An extensive discussion about possible disk line profiles is given in Dumont & Collin-Souffrin (1990). In the first instance, the relative importance of the disk contribution to the core or to the wings depends on the disk inclination. In Fig. 3 we presented simulated profiles, corresponding to $R_{inn} = 400$ Rg, $R_{out} = 1200$ Rg and 12000 Rg, for different inclinations: $i = 1^\circ, 10^\circ, 20^\circ, 40^\circ$ and 60° . As it can be seen in Fig. 3, the contribution of the disk to the center of the line or to the wings is not so much sensitive to the outer radius, but significantly depends on the disk inclination. A face-on disk contributes more to the core of the line, while a moderately inclined disk ($40^\circ > i > 20^\circ$) contributes significantly to the line wings. For $i > 40^\circ$ the disk emission will strongly affect the far wings of the composite profile.

Another very important parameter is the flux ratio between components, Q . As examples, in Fig. 4 we presented five simulations of composite line profiles with values $Q = 0.3, 0.5, 0.7, 1, 1.5$ and 2 , where $R_{inn} = 400$ Rg and $R_{out} = 1200$ Rg, and for different inclinations ($i = 1, 10, 20, 40, 60$ degrees).

We found that the presence of the disk emission is difficult to detect in the line profile when the contribution of the disk is smaller than 30% of the total line emission ($Q > 2$): in the case of a low inclination both the disk and non-disk region contributes to the line core and it is very hard to separate the disk and non-disk region. In the case of a highly inclined disk, the disk emission spreads in the far wings, and could not be resolved from the continuum, especially if the observed spectrum is noisy. For the case of dominant disk emission ($Q < 0.3$), if the inclination is low, the line will be shifted to the red, and if the inclination is high, two peaks or at least shoulders should appear in the composite line profile. Consequently, further in the paper we will consider only cases where $0.3 < Q < 2$.

Note here that, although we have considered a relatively low random velocity of ~ 1000 km/s, the lines where the disk is dominant (the disk contributes at least 50%) can be very broad. The obtained widths are in agreement with the measured widths of double-peaked lines, that range from several thousand (Eracleous & Halpern 1994, 2003) to nearly $40,000$ km s $^{-1}$ (see e.g. Wang et al. 2005, SDSS J0942+0900 has the H α width of ≈ 40000 km s $^{-1}$).

2.5 Results from the line profiles simulations

From the simulations mentioned above we infer the following results:

(i) To detect disk emission in a BELs, the fraction of the flux emitted by the disk in the total line profile should be higher than 30% . A dominant disk ($Q < 0.3$) will be clearly present in the total line profile (peaks or shoulders in the line profiles).

(ii) In the case of a nearly face-on disk ($i < 5^\circ$), the disk emission may contribute to a slight asymmetry towards the red (due to the gravitational redshift), but it is hard to detect this asymmetry. In the case of an edge-on disk, the emission from the disk will contribute to the far wings and then it may be difficult to separate it from the continuum.

(iii) These two parameters, the flux ratio between components and disk inclination, are crucial for the line shapes in the two-component model.

(iv) In the simulated line profiles the asymmetry was mostly $A_i > 0$. For low inclination ($i < 10^\circ$), the asymmetry weakly depends on Q .

3 COMPARISON BETWEEN SIMULATED AND OBSERVED BEL PROFILES

3.1 Data sample and measurements

The set of spectra for our data sample has been collected by La Mura et al. (2007) from the spectral database of the third data release from the Sloan Digital Sky Survey (SDSS)³. According to the purposes of the work (see also La Mura et al. 2007), the SDSS database was searched for sources corresponding to the following requirements: (i) objects were with redshifts $z < 0.4$, so H α would be covered by the available spectral range; (ii) the Balmer series were clearly recognized, at least up to H δ in order to see that in all Balmer lines a broad component is present; (iii) and profiles were not affected by distortions (bad pixels on the sensors, the presence of strong foreground or background sources).

The preview spectra provided by the database retrieval software were manually inspected, looking for objects in better agreement with our requirements, until 115 sources were chosen from approximately 600 candidates examined in various survey areas. Subsequent inspection of the spectra collected within the database led to the rejection of 25 objects, which were affected by problems that could not be detected in the preview analysis. Therefore, our resulting sample includes the spectra of 90 various broad-line-emitting AGN, corresponding to 15% of the candidates that we examined and located in the range.

The spectra were already corrected for instrumental and environmental effects, including sky-emission subtraction and correction for telluric absorption and calibration of data in physical units of the flux and wavelength. Spectra were corrected for the Galactic extinction (see La Mura et al. 2007). Also, the cosmological redshift calibration were performed. Since the interest was to investigate the broad line shapes, the subtraction of the narrow components of H α as well as the satellite [NII] lines were performed. The spectral

³ <http://www.sdss.org/dr3>

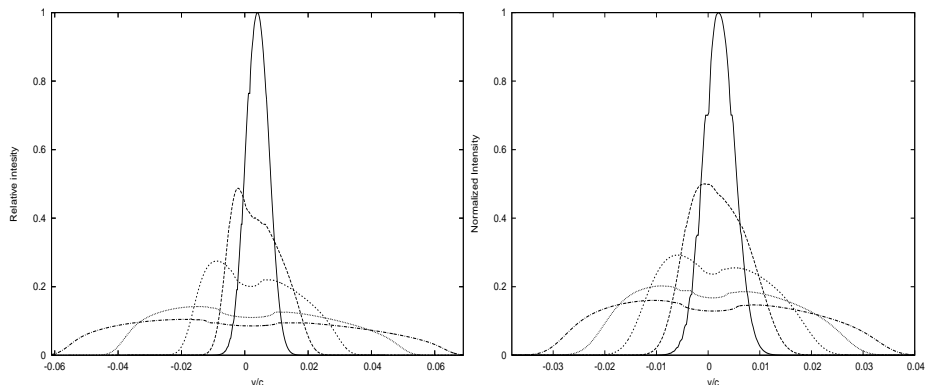


Figure 3. Simulated disk line profiles for five different disk inclinations ($i=1, 10, 20, 40$ and 60 degrees, from the highest to the lowest intensity lines, respectively) for the disk with the fixed inner radius $R_{inn} = 400$ Rg and with outer $R_{out}=1200$ Rg (left) and $R_{out} = 12000$ Rg (right).

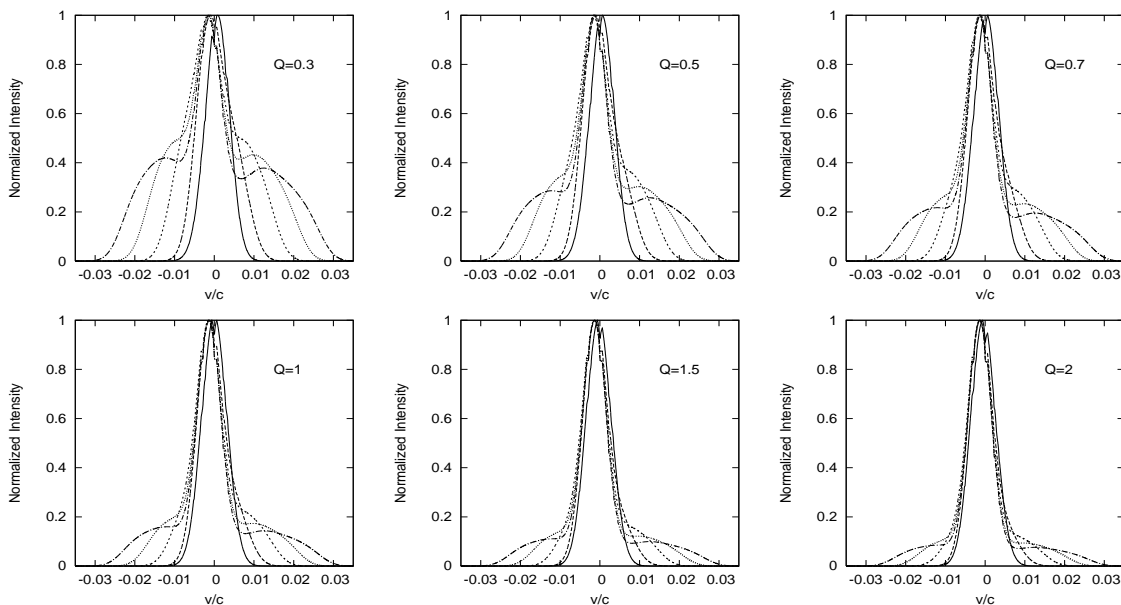


Figure 4. Simulated line profiles emitted by the two-component model for five different inclinations ($i=1, 10, 20, 40$ and 60 degrees, from the narrowest to the broadest line, respectively) for different contributions of the disk to the composite line profiles (as it is written in figures). The inner radius of the disk is taken to be 400 Rg, while the outer radius is 1200 Rg.

reduction (including subtraction of stellar component) and the way to obtain the broad line profiles are in more details explained in La Mura et al. (2007). We have also used FWHM and FWZI measurements from Table 2. of the mentioned paper.

Previously cleaned broad H α profile was normalized, converted from wavelength to velocity scale and smoothed, with Gaussian smoothing, using DIPSO software package⁴. Additionally, we have measured the half (red and blue) widths, W_i^R and W_i^B , at 10%, 20% 30% and 50% of maximum intensity (see Fig. 5), and after that we calculated normalized full widths, k_i , and asymmetries, A_i (Eq. (7)).

3.2 Observed vs. simulated line profiles parameters

In Fig. 6 we presented the normalized widths k_{20} vs. k_{10} and k_{30} vs. k_{10} measured for H α lines of the sample. We also plot the values corresponding to simulations with different disk inclinations, flux ratios Q , and fixed disk dimensions of $R_{inn} = 600$ Rg and $R_{out} = 4000$ Rg. As one can see in Fig. 6, most of the measured points are located within $0.7 < Q < 2$, and $i < 25^\circ$. These results do not change significantly if we change the inner and outer radii of the disk, where the inner radius is not taken to be less than 100 Rg, while the outer was not taken to be closer than several hundreds Rg.

The measured asymmetries of the H α profiles are presented in Fig. 7. Lines in this Figure correspond to the simulated models as in Fig. 6. As it can be seen in Fig. 7, some objects (around 10 objects from the sample of measured H α lines) have a high negative asymmetry which cannot be explained by assumed models without a systemic motion of the

⁴ <http://www.starlink.rl.ac.uk>

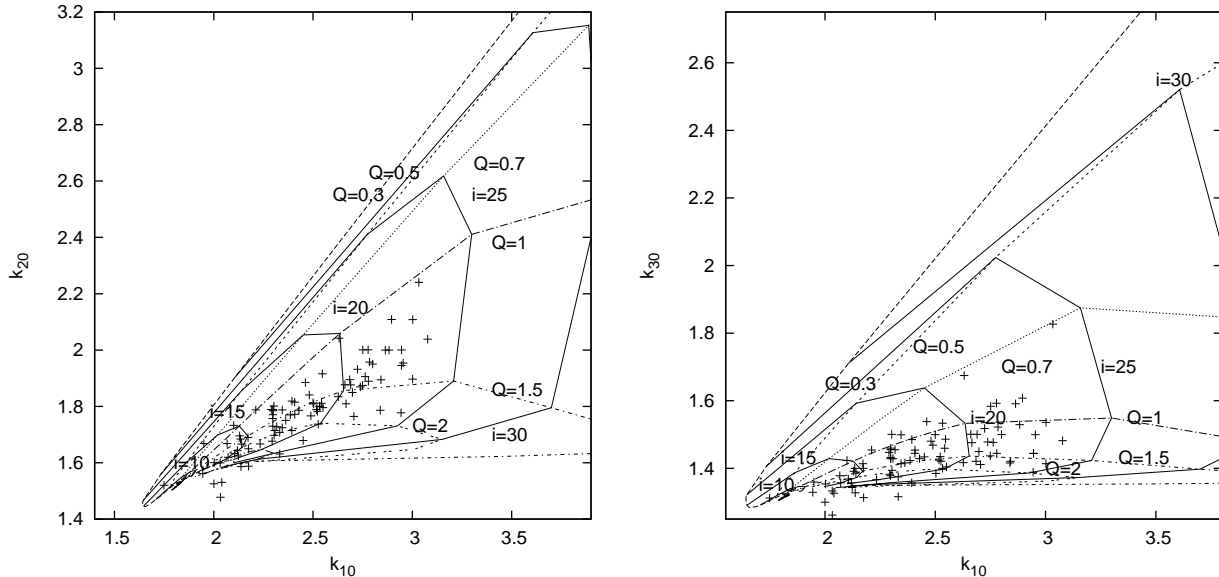


Figure 6. The measured width ratios (crosses) and simulated values (dashed lines) from the two-component model for the different contribution of the disk emission to the total line flux ($Q=0.3, 0.5, 0.7, 1, 1.5$ and 2). The inner disk radius is taken to be $600 R_g$, outer $4000 R_g$, and different inclinations are considered (solid isolines presented $i = 10, 15, 20, 25$ and 30 degrees, respectively).

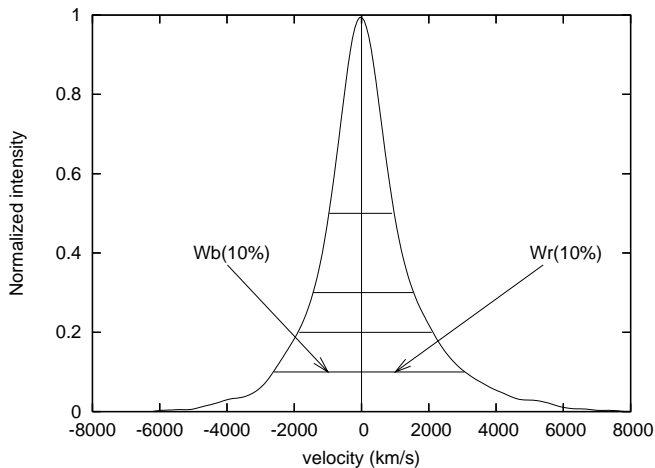


Figure 5. The broad $H\alpha$ line of SDSSJ1025+5140. The horizontal lines presented the measured widths at 10%, 20%, 30% and 50% of the maximum intensity. The blue and red half widths have been measured.

non-disk region. To explore the outflow or inflow presence (to explain the blue asymmetry of the core component), we consider shifts of the Gaussian component in the model. As it can be seen in Fig. 7 (bottom) models where a blueshift of the Gaussian component of 800 km s^{-1} was taken into account (other parameters are not changed), are able to explain the measured asymmetries.

As it can be seen in Fig. 6, the coefficients k are sensitive to the disk inclination and Q , therefore we will use the relationships between these coefficients to give some estimates of the inclination and Q for the sample. Of course, we should also take into account the influence of the disk dimensions. To do that we compute a grid of models with $k_i = f(R_{inn}, i, Q)$ confirming that the changes in the param-

eters mainly depend on i and Q . We found that for inner radius $R_{inn} < 200 R_g$, the simulated k_i do not fit well the observations (most of the measured points from the sample are out of the grid of models, as it is presented in Fig. 6). The same inconsistencies are found for $R_{out} < 1000 R_g$.

In order to derive some results about the disk parameters we assume the following constraints and procedures:

i) According to the results obtained from the fitting of the double-peaked lines in Eracleous & Halpern (2003) we fixed the inner radius at $R_{inn}=600 R_g$, and the outer at $R_{out}=4000 R_g$, as the averaged values obtained from their fittings (Eracleous & Halpern 2003).

ii) For each AGN in the sample we estimate i and Q using the normalized widths, k_i . Specifically, we obtain two estimates for i and Q as the values associated to the measurements of both k_{10} vs. k_{20} and k_{10} vs. k_{30} . In Table 1 we present the averaged values and differences between those estimates, Δi , and ΔQ for the case without blue shift of the non-disk component..

iii) We excluded from the analysis the objects where difference between estimated i and Q was huge, in total 5 objects where the two-component model cannot be applied. Also there are 9 objects $\Delta i > 1$ degree (presented as full triangles in Fig. 8 and in Figs. after). In Fig. 8, we present the k_i parameters as function of the inclination. As one can see, most of the points are well concentrated as a linear function of i vs. k_i .

In Fig. 9, we present histograms of the number of AGN vs. i and Q . As one can see in Figure, there is a peak at $i \sim 17^\circ$ while estimated values are within $10^\circ < i < 25^\circ$ in both cases: without (solid line) and with systematic blue shift of the non-disk (see Fig. 7). Also, there is a peak at $Q \sim 1.25$ and most of the points are within $1 < Q < 2$, showing that the disk emission is typically smaller than the emission of the non-disk region.

One can expect randomly oriented accretion disk in

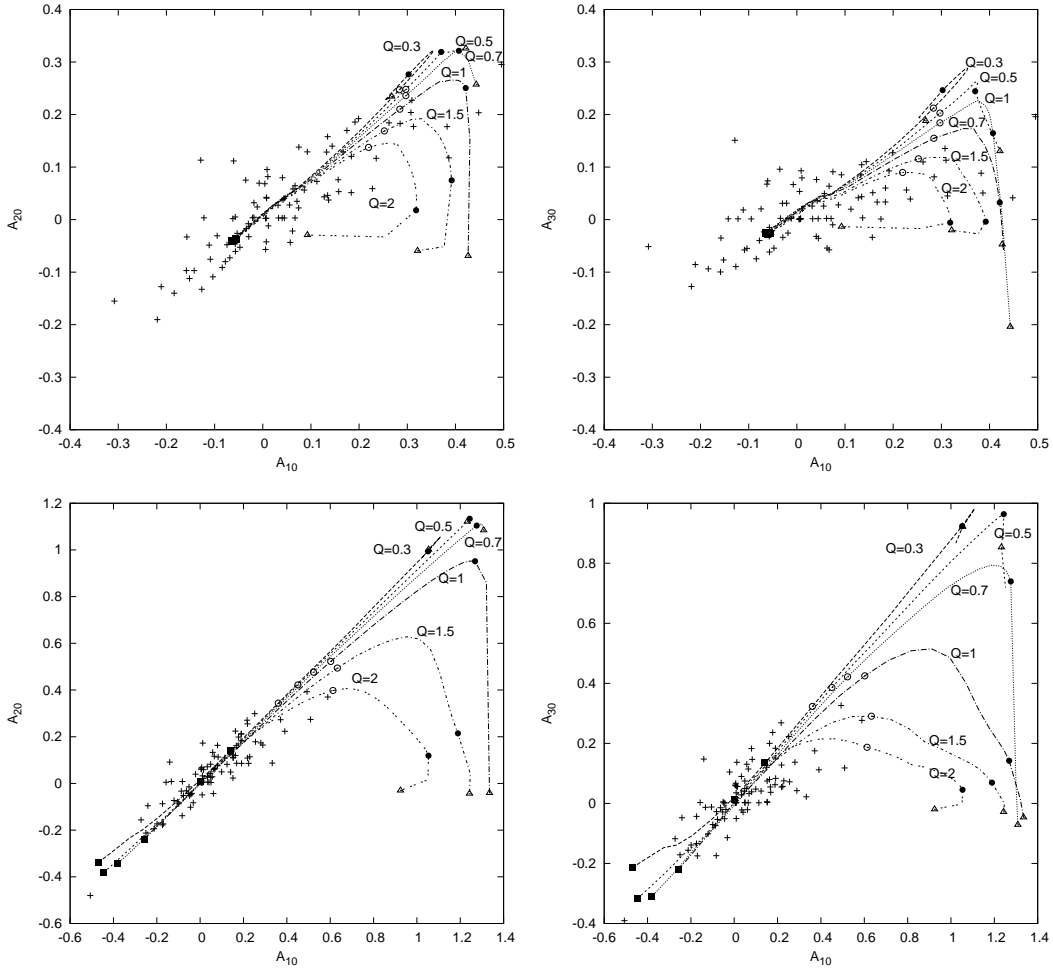


Figure 7. The asymmetry of the $H\alpha$ line of the sample (crosses) and simulated one from the two-component model. Different contributions of the disk emission to the total line flux (Q) are taken into account, and plotted with a dashed lines ($Q=0.3, 0.5, 0.7, 1, 1.5$ and 2). The inner disk radius is taken to be $600 R_g$ and outer $4000 R_g$. Different inclinations are considered, taking values from 0 (full squares), 10 (open circles), 20 (full circles) and 30 (open triangles) degrees. On two panels up we presented the models without systematic shift of the non disk component, while on two panels bottom, a systematic blue shift of 800 km/s was taken into account.

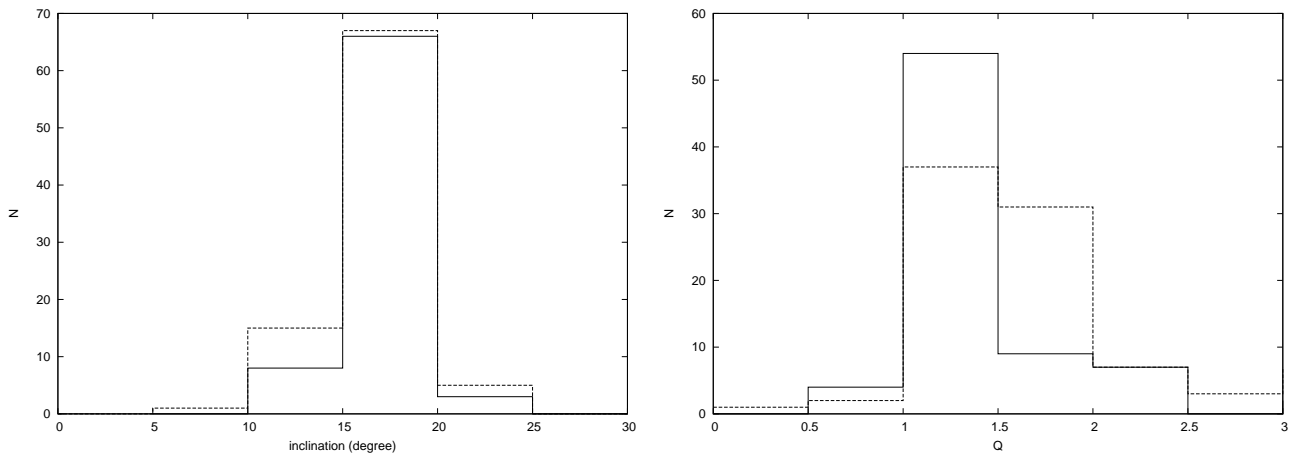


Figure 9. Histograms of the inclination (left) and $Q = F_s / F_{disk}$ (right) for the sample in the case with (dashed line) and without (solid line) systematic blue shift of the non-disk component (see Fig. 7). The cases where discrepancy in the inclination were more than one degree, were not taken into account.

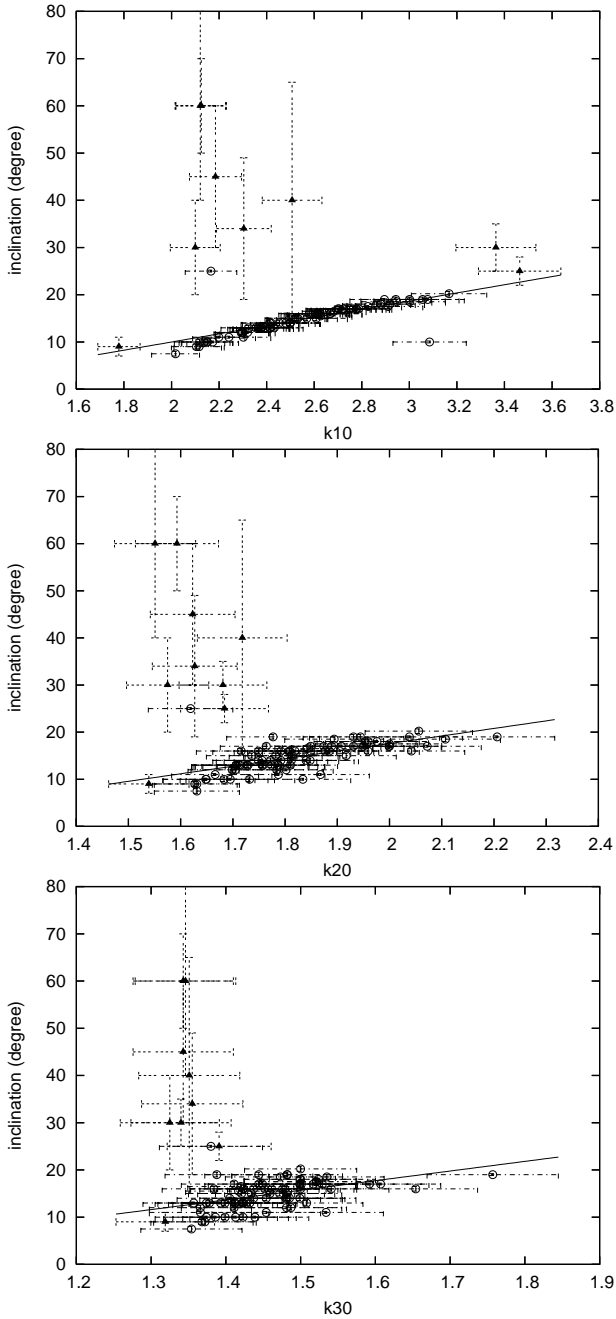


Figure 8. Inclination vs. k_{10} (the first), k_{20} (the second) and k_{30} (the third). The points where description were more than one degree (mainly above the other points) are denoted with full triangles.

AGN, but we obtained low inclined disk. Such small inclination range ($10^\circ < i < 25^\circ$), may be expected since a highly inclined disk has a smaller brightness than surrounding non-disk region. Therefore one can expect a weak disk emission in far wings which cannot be detected.

4 DISCUSSION

In the previous sections we have made a grid of two-component models, aiming to search for the hidden disk

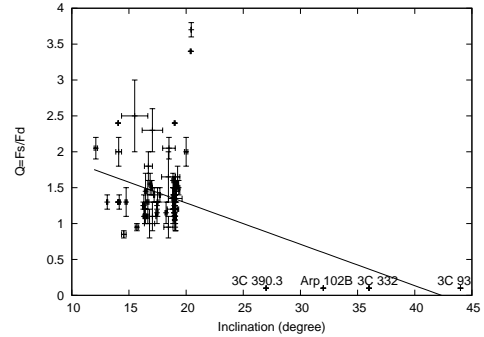


Figure 10. Q vs. inclination for the sample, and the position of the well known AGN with double-peaked lines (Eraclous & Halpern 1994), where is assumed that in these objects $Q < 0.1$.

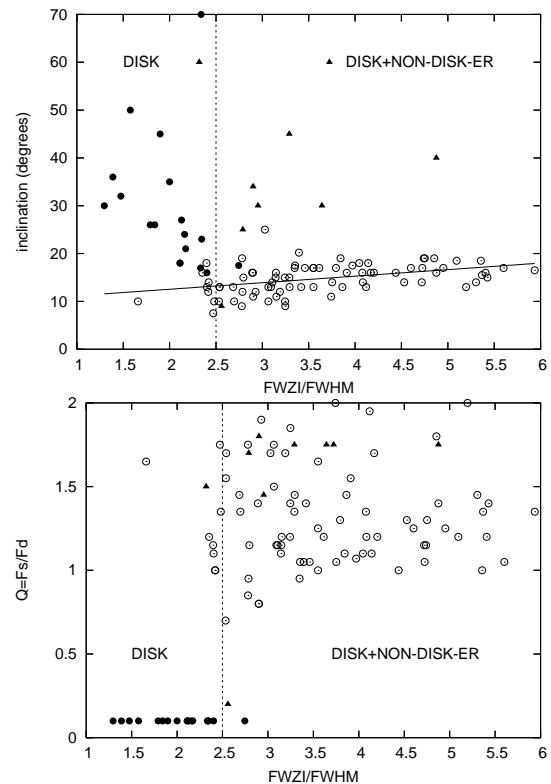


Figure 11. Inclination (top) and Q (bottom) as function of the $FWZI/FWHM$. With full points the measurements of the disk parameters and widths are taken from Eraclous & Halpern (1994,2003), and open circles are from the sample (measurements of the FWHM and FWZI are taken from La Mura et al. 2007). The vertical dashed line shows a rough border between disk emission lines and ones where the disk may be superposed with the emission of an additional region.

emission. We found that the more significant parameters in the generation of the emission line profiles are the inclination and the flux ratio between components, Q . On the other hand, we have also explored the influence of the inner radius. Comparing a grid of simulated line profiles with the data of the 90 AGN sample from SDSS, we found that, if the disk emission is present, the inner radius should not

be smaller than $200 R_g$ (it seems to be in the range $1000 R_g > R_{inn} > 200 R_g$)⁵.

Fixing the inner and outer radius to an averaged value, obtained from the study of BELs with two-peaked lines (Eracleous & Halpern 2003), we estimated the values of i and Q for the 90 AGN sample from SDSS. According to Table 1 (where we give data for the case without systematic blue shift of the non-disk component) and the histogram in Figure 9, the two component model associates significant disk emission to practically all objects.

In Figure 10 we present Q vs i , with well known double peaked AGN, assuming that the contribution of the non-disk region is smaller than 10%. Note here, that even in double-peaked emitters, there is often a residual, so called 'classical broad line' component left over after the disk fit (as e.g. in 3C390.3, see Eracleous & Halpern 2003). In this case, there is an indication that the linear regression may be present in Q vs. i . This may be caused by the disk brightness, i.e. with higher inclinations the disk emission decreases (Eq. 2) and in this case, the disk emission can be detected if the non-disk emission is negligible.

As an additional test, we have used measurements of the FWHM and FWZI (La Mura et al. 2007) for the 90 AGN sample from SDSS and for double peaked lines by Eracleous & Halpern (1994, 2003) to plot the inclination, i , vs. $FWZI/FWHM$. As it can be seen in Fig. 11, there is a clear separation between single and double-peaked lines (except for the points for which we estimate Q and i with high uncertainty, presented as full triangles). This also indicates that a high inclined disk emission can be detected if it is more dominant than the non-disk component. Note here that the lack of AGN population with $Q < 1$ (see Fig. 11) is probably caused by selection effects, since we selected a sample where single-peaked profile is dominant.

The problem of a low-inclined disk ($i < 25^\circ$), that we obtained from this sample of AGN, still remains. The restriction on inclination is problematic for disk models, since we may expect random orientations - at least within the range allowed by the torus opening angle (given that the accretion disk and torus are co-axial, see Fig. 12). Then high-inclined disks may be obscured by the torus, but in this case one can expect the cut-off in the inclination around 45° - 50° . One explanation may be that we have situation as schematically presented in Fig. 12, where the disk is co-axial with the torus, and there are three cases depending on the line-of-sight of an observer; 1) line-of-sight is throughout the torus, where the disk and non-disk regions are obscured and one can detect only narrow lines, 2) as inclination stay smaller, the non-disk contribution stay important, but the disk emission is still full or partly obscured (very close to the torus one can expect absorbing material able to absorb disk emission and partly non-disk emission); and 3) for a low-inclined disk the absorption coming from the torus is negligible, then disk and non-disk emission can be fully detected.

In the case 2), the fraction of the disk emission may be too weak. Consequently, it is very hard to extract possible

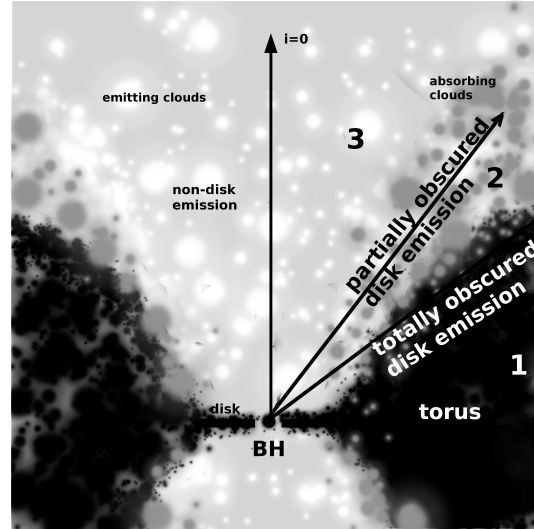


Figure 12. Obscuration of the disk emission: 1)torus, 2)absorbing material around the torus and 3) the region without absorption (see text in §5).

disk parameters (see Fig 8, the dots denoted as triangles mainly have higher inclinations than 25 degrees).

5 CONCLUSIONS

Here we investigated the hidden disk emission in single peaked line profiles of type 1 AGN in order to find any indication that the disk emission is present in non double peaked broad lines.

Finally, we outline the following conclusions:

1) As it was mentioned earlier (Popović et al. 2004; Bon et al. 2006), a two component model (disk + non-disk region) can well describe the majority of the observed single peaked line profiles.

2) After comparing simulated and observed line profiles, there is an indication that the disk emission may be present also in single peaked broad line profiles, but it is mainly smaller than 50% of the total line flux.

3) The estimated inclination of the disk indicates a low inclined disk, with inclinations $i < 25^\circ$ that might be caused by the torus and/or absorbing material around the torus.

4) In some of the observed $H\alpha$ line profiles there is a blue asymmetry that can be fitted considering a blue-shift of the non-disk region of ~ 800 km/s. This may indicate an outflow in the non-disk region in some AGN from the sample.

ACKNOWLEDGMENTS

Acknowledgments. The work was supported by the Ministry of Science of Serbia through the project 146002: ‘‘Astrophysical spectroscopy of extragalactic objects’’. We would like to thank to the referee for very useful comments

REFERENCES

Baird S.R., 1981, ApJ, 245, 208.

⁵ Taking $R_{inn} < 200 R_g$ or $R_{inn} > 1000 R_g$ we could not find a grid of models, like shown in Fig. 6, that fit the measured k_i parameters

Bon, E., Popović, L. Č., Ilić, D., Mediavilla, E.G., 2006, *NewAstRev*, 50, 716.

Bon, E., 2008. *SerAJ*, 177.

Cao, X and Wang, T.-G. 2006, *ApJ*, 652, 112

Chen, K. & Halpern, J.P. 1989, *ApJ*, 344, 115.

Chen, K., Halpern, J.P. & Filippenko, A.V. 1989, *ApJ*, 339, 742.

Collin, S., Kawaguchi, T., Peterson, B. M., Vestergaard, M. 2006, *A&AS*, 456, 75

Corbin, M. R. & Boroson, T. A. 1996, *ApJS*, 107, 69.

Dumont, A.M. & Collin-Souffrin, S. 1990, *A&AS* 83, 71.

Eracleous, M. & Halpern, J.P. 1994, *ApJS*, 90, 1.

Eracleous, M. & Halpern, J.P. 2003, *ApJ*, 599, 886.

Ho, L.C., Rudnick, G., Rix, H.-W. et al. 2000, *ApJ* 541, 120.

Hu, C. , Wang, J. M., Chen, Y. M., Bian W. H., Xue S. J., 2008, *ApJ*, 683L, 115H

Ilić, D., Popović, L.Č., Bon, E. Mediavilla, E. G., Chavushyan, V. H. 2006, *MNRAS*, 371, 1610

Jovanović, P. & Popović L.Č., 2008, *Fortschr. Phys.* 56, No. 4 - 5, 456.

Kollatschny, W. & Bischoff, K. 2002, *A&A*, 386, L19.

Kollatschny, W. 2003, *A&A*, 407, 461

La Mura, G., Popović, L. Č., Ciroi, S., Rafanelli, P., Ilić, D. 2007, *ApJ*, 671, 104L

La Mura, G.; Mille, F. Di; Ciroi, S.; Popović, L. Č.; Rafanelli, P., 2009. *APJ*, 639, 1437.

Livio, M. & Xu, C. 1997, *ApJ*, 478, L63.

Marziani, P., Sulentic, J. W., Stirpe, G. M., Zamfir, S., Calvani, M. 2009, *A&A*, 495, 83

Murray, N. & Chiang, J. 1995, *ApJ*, 454, 105.

Murray, N. & Chiang, J. 1997, *ApJ*, 474, 91.

Murray, N. & Chiang, J. 1998, *ApJ*, 494, p.125.

Perez, E., Mediavilla, E., Penston, M. V., Tadhunter, C., Moles, M. 1988, *MNRAS*, 230, 353.

Popović, L. Č., A. A. Smirnova, J. Kovačević, A. V. Moiseev, and V. L. Afanasiev, 2009, *AJ*, 137, 3548.

Popović, L. Č., Bon, E., Gavrilović N., 2008, *RevMexAA SC*, 32, 99.

Popović, L. Č., Mediavilla, E.G., Bon, E., Ilić, D., 2004, *A&A*, 423, 909.

Popović, L. Č., Mediavilla, E.G., Bon, E., Stanić, N., Kubičela, A., 2003, *ApJ*, 599, 185.

Popović, L. Č., Mediavilla, E.G., Kubičela, A., Jovanović, P., 2002, *A&A*, 390, 473.

Popović, L. Č., Stanić, N., Kubičela, A., Bon, E. 2001,*A&A*, 367, 780.

Proga, D. and Kallman, T. R., 2004, *ApJ*, 616, 688

Rodríguez-Ardila, A., Pastoriza, M.G., Bica, E. 1996, *ApJ*, 463, 522.

Rokaki, E. & Boisson, C. 1999, *MNRAS* 307, 41.

Romano, P, Zwitter, T., Calvani, M., Sulentic, J. 1996, *MNRAS*, 279, 165.

Smith, J. E., Robinson, A., Young, S., Axon, D. J., Corbett, Elizabeth A. 2005, *MNRAS*, 359, 846S.

Shapovalova, A. I., Doroshenko, V. T., Bochkarev, N. G., Burenkov, A. N., Carrasco, L., Chavushyan, V. H., Collin, S., Valdes, J. R., Borisov, N., Dumont, A.-M., Vlasuyk, V. V., Chilingarian, I., Fiohtistova, I. S., Martinez, O. M., 2004, *A&A*, 422, 925

Shields, J.C., Rix, H.-W., McIntosh, D.H. et al. 2000, *ApJ* 534, L27.

Storchi-Bergmann, T., Eracleous, M., Ruiz, M.T., Livio, M., Wilson, A.S. & Filippenko, A.V. 1997, *ApJ*, 489, 87.

Storchi-Bergmann, T., Nemmen, R., Eracleous, M., Halpern, J. P., Filippenko, A. V., Ruiz, M. T., Smith, R. C., Nagar, N. 2003a, *ApJ*, 598, 956.

Storchi-Bergmann, T. de Silva, R.N., Eracleous, M. 2003b, *ASPC*, 290, 155

Strateva, I.V., Strauss, M.A., Hao, L. et al. 2003, *AJ*, 126, 1720

Sulentic, J. W., Marziani, P. & Zamfir, N.S. 2009, will appear in *New. Astr. Rev.* doi:10.1016/j.newar.2009.06.001

Sulentic, J. W., Marziani, P. & Dultzin-Hacyan, D. 2000, *ARAA* 38, 521.

Urry M. C. & Padovani P. 1995, *PASP* 107, 803.

Wang, J.-M. Ho, L. C., Staubert, R. 2003, *A&A*, 409, 887.

Wang, T.-G., Dong, X.-B., Zhang, X.-G., Zhou, H.-Y., Wang, J.-X., Lu, Y.-J. 2005, *ApJ*, 625, L35

Wills, B. J., Brotherton, M. S., Fang, D., Steidel, C. C., & Sargent, W. L. W. 1993, *ApJ*, 415, 563

APPENDIX A: THE CASES OF THE DIFFERENT GAUSSIAN WIDTHS

As we mentioned in §2.2, we fixed the widths of Gaussian (that represents the non-disk component) to $\sigma = 1000$ km/s. Recall the results of Popović et al. (2004) and Bon et al. (2006), where the σ of the Doppler broadening from the non disk component (the Gaussian representing ILR) were estimated to be from 300 to 1700 km/s. This is in a good agreement with the results of Hu et al. (2008). They used a two component model assuming that a broad line can be represented by two Gaussians (one very broad, and another with intermediate velocities, corresponding to ILR and VBLR respectively) that FWHM's from VBLR and ILR components are in correlation, as $\text{FWHM(ILR)} \sim 0.4 \text{ FWHM(VLBR)}$, and FWHM (ILR) ranged from 1000 to 4000 km/s ($\sigma \sim 400$ to ~ 1700 km/s) (Hu et al. 2008).

But, to have an impression how σ of the non-disk component can affect composite profiles, we performed simulations using different σ . We started from $\sigma \sim 400$ to ~ 1700 km/s which corresponds $\text{FWHM} \sim 1000$ to ~ 4000 km/s, with a step of $\Delta \text{FWHM} = 1000$ km/s. The disk parameters are taken as $R_{inn}=600 R_g$, $R_{out}=4000 R_g$, emissivity $p = 3$, and we considered different inclinations and Q . In Figs. A1-A3 we presented calculated parameters k_{20} , k_{30} vs. k_{10} for $Q=0.3, 1$ and 2 , taking $\sigma = 500$ km/s, 1000 km/s and 1700 km/s and different inclinations. Also, the elliptical surface shown in Figs. A1-A3 presents the surface where the measured data from the sample are located. As one can see, different values of σ can affect obtained results for Q and inclination, but it is interesting that measured data indicates $\sigma \sim 1000$ km/s well fit the surface of measured values in all three considered cases. Also, for the very broad non-disk component ($\sigma > 1700$ km/s) it is hard to use this model to estimate the disk parameters (especially for small inclinations).

Table 1. Measured k and estimated inclination and ratio of contributions of the non-disk and disk emission.

SDSS name	redshit	k_{10}	k_{20}	k_{30}	i	Δi	Q	ΔQ
SDSSJ1152-0005	0.276	3.03	2.24	1.83	19	0.05	1.05	0.05
SDSSJ1157-0022	0.178	2.36	1.75	1.42	17	0.05	1.5	0.1
SDSSJ1307-0036	0.188	2.90	2.11	1.61	19	0.05	1.15	0.05
SDSSJ1059-0005	0.282	2.72	1.93	1.52	18.95	0.01	1.2	0.01
SDSSJ1342-0053	0.129	2.76	1.91	1.48	18.95	0.01	1.2	0.01
SDSSJ1307+0107	0.26	2.84	1.79	1.42	19	0.05	1.35	0.05
SDSSJ1341-0053	0.17	2.52	1.79	1.42	19.35	0.1	1.5	0.1
SDSSJ1344+0005	0.276	2.30	1.77	1.43	16.25	0.01	1.25	0.05
SDSSJ1013-0052	0.326	2.14	1.67	1.39	17.35	3.2	1.45	0.05
SDSSJ1010+0043	0.237	2.30	1.80	1.50	16.8	0.45	1	0.2
SDSSJ1057-0041	0.0871	2.03	1.60	1.33	17.25	3.0	3.3	0.3
SDSSJ0117+0000	0.245	2.78	2.00	1.59	19	0.05	1.1	0.01
SDSSJ0112+0003	0.0737	3.08	2.04	1.48	18.95	0.01	1.15	0.05
SDSSJ1344-0015	0.14	2.39	1.71	1.36	18.5	0.55	2.05	0.15
SDSSJ1343+0004	0.114	2.48	1.84	1.48	18.25	0.1	1.15	0.15
SDSSJ1519+0016	0.232	2.30	1.79	1.46	16.4	0.15	1.1	0.1
SDSSJ1437+0007	0.179	2.43	1.79	1.43	17.7	0.05	1.4	0.1
SDSSJ1619+6202	0.31	2.18	1.59	1.31				
SDSSJ0121-0102	0.359	2.17	1.65	1.40	15.15	0.5	1.75	0.45
SDSSJ1719+5937	0.174	2.55	1.80	1.40	18.95	0.01	1.5	0.01
SDSSJ1717+5815	0.279	2.07	1.62	1.36	14.05	0.01	2.4	0.01
SDSSJ0037+0008	0.362	2.86	2.00	1.59	18.95	0.01	1.15	0.05
SDSSJ2351-0109	0.252	2.07	1.67	1.38	13.1	0.05	1.3	0.1
SDSSJ2349-0036	0.0456	2.21	1.79	1.45	15.7	0.15	0.95	0.05
SDSSJ0013+0052	0.239	2.31	1.71	1.43	16.45	0.1	1.45	0.25
SDSSJ1720+5540	0.0543	2.14	1.59	1.33				
SDSSJ0256+0113	0.0804	1.75	1.52	1.31	13.2	3.95	0.3	0.01
SDSSJ0135-0044	0.334	1.94	1.56	1.33				
SDSSJ0140-0050	0.146	2.66	1.88	1.50	19	0.05	1.25	0.05
SDSSJ0310-0049	0.217	2.13	1.70	1.39	14.05	0.01	1.3	0.01
SDSSJ0304+0028	0.368	1.95	1.67	1.36	12.95	2.3	0.9	0.4
SDSSJ0159+0105	0.198	2.54	1.81	1.46	18.85	0.1	1.35	0.15
SDSSJ0233-0107	0.177	2.30	1.78	1.46	16.4	0.15	1.1	0.1
SDSSJ0250+0025	0.0445	2.71	1.76	1.41	19.05	0.01	1.4	0.1
SDSSJ0409-0429	0.0802	2.30	1.76	1.43	16.3	0.05	1.25	0.15
SDSSJ0937+0135	0.107	2.35	1.72	1.41	16.85	0.1	1.55	0.15
SDSSJ0323+0035	0.185	2.69	1.88	1.50	19	0.05	1.25	0.05
SDSSJ0107+1408	0.215	2.95	1.95	1.50	18.95	0.01	1.2	0.01
SDSSJ0142+0005	0.0768	2.53	1.80	1.40	19.1	0.15	1.55	0.05
SDSSJ0306+0003	0.0941	2.95	1.94	1.44	18.95	0.01	1.2	0.01
SDSSJ0322+0055	0.0893	2.95	2.00	1.44	19	0.05	1.2	0.01
SDSSJ0150+1323	0.0371	2.63	2.04	1.67	19.05	0.01	0.95	0.05
SDSSJ0855+5252	0.0691	2.75	1.87	1.44	19.05	0.01	1.3	0.01
SDSSJ0904+5536	0.0388	2.41	1.81	1.44	17.45	0.01	1.25	0.05
SDSSJ1355+6440	0.0505	2.80	1.95	1.50	18.95	0.01	1.2	0.01
SDSSJ0351-0526	0.0751	2.29	1.68	1.38	18.4	1.75	1.95	0.05
SDSSJ1505+0342	0.0583	2.67	1.81	1.48	18.95	0.01	1.3	0.1
SDSSJ1203+0229	0.0931	2.30	1.73	1.38	16.7	0.35	1.8	0.2
SDSSJ1246+0222	0.0775	2.11	1.63	1.37	14.1	0.25	2	0.2
SDSSJ0839+4847	0.0236	2.13	1.68	1.40	14.15	0.1	1.3	0.1
SDSSJ0925+5335	0.0867	2.78	1.89	1.44	19	0.05	1.25	0.05
SDSSJ1331+0131	0.0482	2.94	1.78	1.39	19	0.05	1.35	0.05
SDSSJ1042+0414	0.0805	6.82	1.58	1.36	19.05	0.01	1.3	0.01
SDSSJ1349+0204	0.0328	2.55	1.92	1.49	19.05	0.1	1.1	0.1
SDSSJ1223+0240	0.0722	2.17	1.69	1.41	14.75	0.1	1.3	0.2
SDSSJ0755+3911	0.0335	2.41	1.77	1.45	17.5	0.05	1.3	0.2
SDSSJ1141+0241	0.0459	2.78	1.96	1.52	19	0.05	1.2	0.01
SDSSJ1122+0117	0.0394	2.70	1.85	1.45	19	0.05	1.25	0.05
SDSSJ1243+0252	0.0767	2.50	1.81	1.50	18.85	0.5	1.2	0.2
SDSSJ0832+4614	0.0605	3.00	1.90	1.41	19	0.05	1.25	0.05
SDSSJ0840+0333	0.0525	2.04	1.53	1.33				
SDSSJ1510+0058	0.0359	2.35	1.79	1.50	17.05	0.3	1.1	0.2

Table 1. continued

SDSSJ0110-1008	0.078	2.39	1.82	1.49	17.45	0.1	1.15	0.15
SDSSJ0142-1008	0.0303	2.33	1.63	1.32	19	0.05	2.4	0.01
SDSSJ1519+5208	0.0693	2.53	1.74	1.42	18.85	0.1	1.6	0.1
SDSSJ0013-0951	0.0738	2.53	1.80	1.53	19.1	0.15	1.2	0.3
SDSSJ1535+5754	0.0615	2.12	1.64	1.36	15.5	1.15	2.5	0.5
SDSSJ1654+3925	0.0419	2.23	1.67	1.37	17.05	0.9	2.3	0.3
SDSSJ0042-1049	0.0581	2.52	1.78	1.43	19.15	0.3	1.45	0.15
SDSSJ2058-0650	0.0904	2.50	1.81	1.38	19.25	0.2	1.65	0.15
SDSSJ1300+6139	0.0522	2.10	1.73	1.42	14.55	0.2	0.85	0.05
SDSSJ0752+2617	0.0948	2.74	1.87	1.48	19	0.05	1.25	0.05
SDSSJ1157+0412	0.0822	2.84	1.89	1.42	19	0.05	1.25	0.05
SDSSJ1139+5911	0.0854	2.30	1.70	1.39	18.55	1.7	1.75	0.15
SDSSJ1345-0259	0.0279	2.00	1.53	1.30	20.45	0.01	3.7	0.1
SDSSJ1118+5803	0.0613	2.32	1.73	1.46	16.65	0.1	1.3	0.3
SDSSJ1105+0745	0.0734	2.45	1.68	1.43	18.45	0.6	1.65	0.35
SDSSJ1623+4804	0.0449	2.33	1.71	1.37	20	0.15	2	0.2
SDSSJ0830+3405	0.0696	2.00	1.60	1.35	12.1	0.15	2.05	0.15
SDSSJ1619+4058	0.0335	2.12	1.62	1.34	17.75	1.6	3.1	0.3
SDSSJ0857+0528	0.0379	2.39	1.77	1.42	17.2	0.05	1.4	0.1
SDSSJ1613+3717	0.0586	2.49	1.77	1.47	19.05	0.6	1.35	0.25
SDSSJ1025+5140	0.0623	3.00	2.11	1.54	19	0.05	1.15	0.05
SDSSJ1016+4210	0.0553	2.63	1.83	1.42	19.05	0.01	1.35	0.05
SDSSJ1128+1023	0.0504	2.88	2.00	1.53	18.95	0.01	1.15	0.05
SDSSJ1300+5641	0.0718	2.75	2.00	1.58	19	0.05	1.1	0.01
SDSSJ1538+4440	0.0406	2.29	1.79	1.45	18.2	2.05	1.1	0.1
SDSSJ1342+5642	0.0728	2.46	1.88	1.54	18.45	0.4	0.95	0.15
SDSSJ1344+4416	0.0547	2.68	1.89	1.42	19	0.05	1.25	0.05
SDSSJ1554+3238	0.0483	2.03	1.48	1.26	20.4	0.05	3.4	0.01

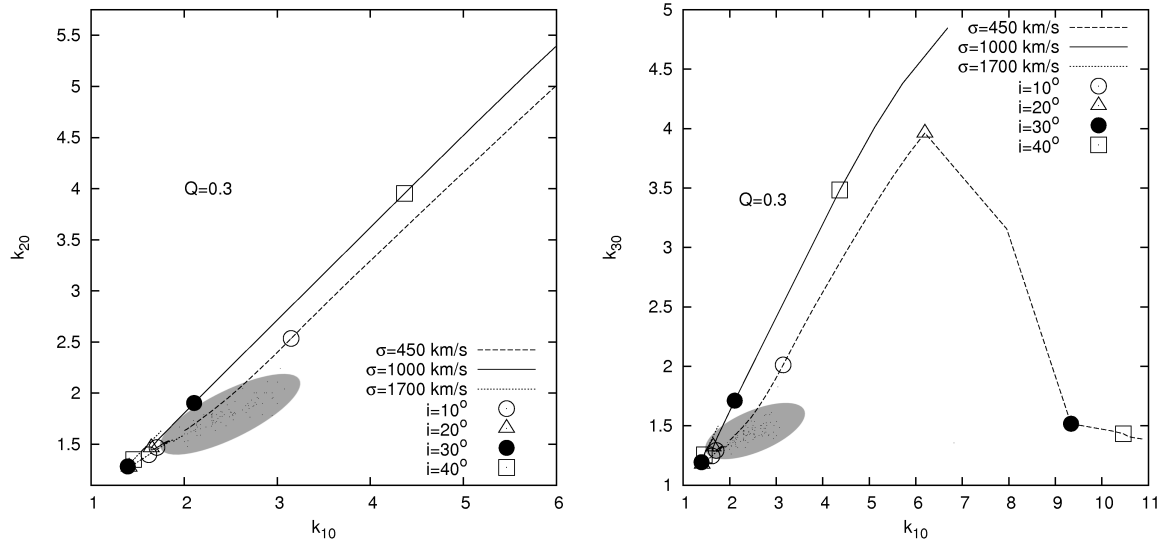


Figure A1. Simulated k_{20} vs. k_{10} (left) and k_{30} vs. k_{10} (right) for different σ for the non-disk component. The elliptical surface denotes the surface of measured values from the sample. The disk parameters are taken as: $R_{in}=600 R_g$, $R_{out}=4000 R_g$, $\sigma_d=1000$ km/s

APPENDIX B: THE TWO-COMPONENT MODEL VS. TWO-GAUSSIAN FITTING

As we mentioned above, there are several possibilities for the BLR geometry, i.e. for geometry of the VBLR and ILR. In principle, there are many analyzes based on two broad Gaussian in order to explain physics and geometry of the BLR (see e.g. Marziani et al. 2009).

Here we briefly discuss the fitting using the two-

component model (as it was described in Popović et al. 2004) and two Gaussians. As an example here we show the best fit with the two-component model (Fig. B1a, left) and with the two-Gaussian one (Fig. B1b). As one can see in Fig. B1, both models can well fit the complex line profiles. The obtained kinematical parameters are: 1) two-Gaussian $FWHM_{VBLR}=3760$ km/s (redshifted ~ 560 km/s), $FWHM_{ILR}=1390$ km/s (in the center) and $Q=F_{ILR}/F_{VBLR} \approx 0.6$; 2) two-component model with the

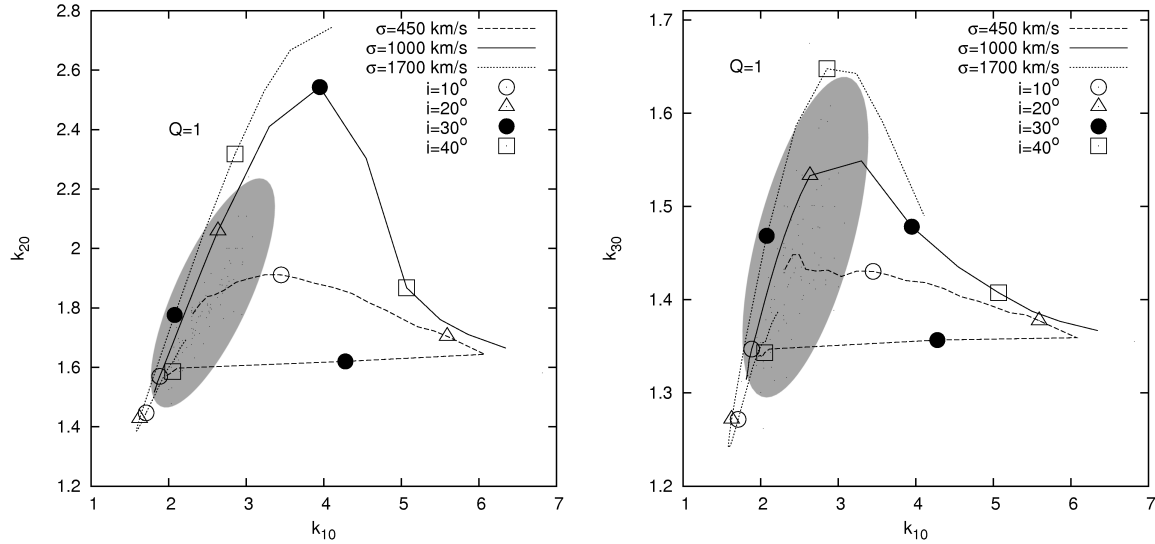


Figure A2. The same as in Fig 13, but for $Q=1$.

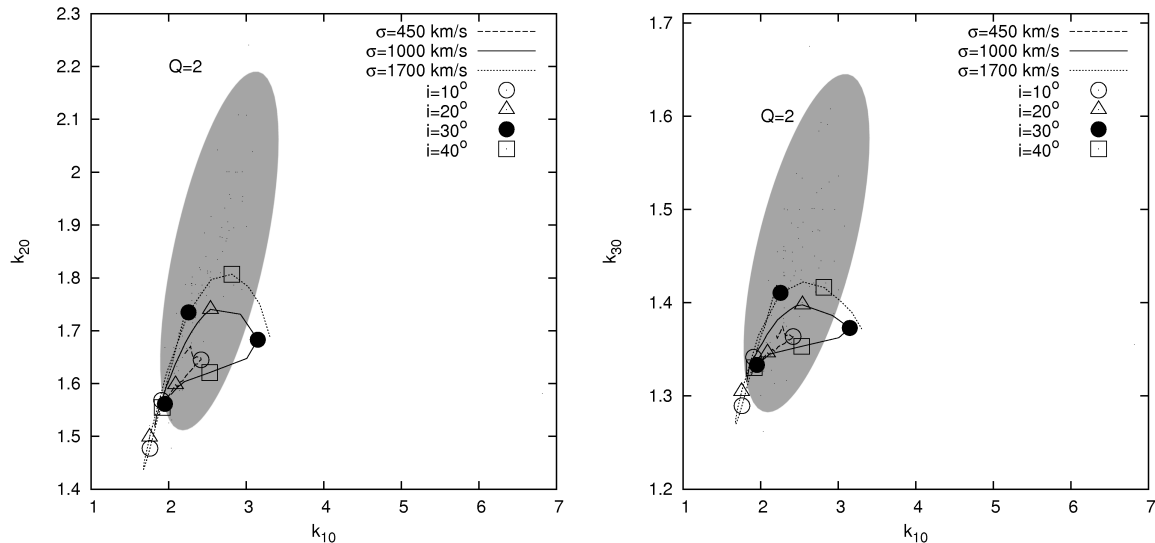


Figure A3. The same as in Fig 13, but for $Q=2$.

disk emission $\text{FWHM}_{\text{Disk}} = 1620$ km/s (redshifted ~ 0 km/s), $\text{FWHM}_{\text{ILR}} = 1360$ km/s and $Q = \text{F}_{\text{ILR}}/\text{F}_{\text{Disk}} \approx 0.8$. The obtained kinematical parameters in both cases indicate that VBLR has higher velocities, but in the case of the assumed disk emission the random velocity is comparable with one present in the ILR.

Comparing the VBLR Gaussian and disk component we found that mainly the VBLR Gaussian should be shifted to the red in order to fit complex BEL profiles (similar as in the case of so called Pop B objects, see Sulentic et al. 2009), while the disk component is more consistent with the ILR component.

Additionally, we did several tests taking into account the two-Gaussian model, fixing one that represents the ILR emission at $\text{FWHM} = 1000$ km/s, and changing the width of the one representing the VBLR from 1000 km/s to 10000 km/s taking different $Q = \text{F}_{\text{ILR}}/\text{F}_{\text{VBLR}} = 0.3, 0.5, 1, \text{ and } 2$

(see Fig. B2). We also measured k_i for such modeled profiles and compared them with measured from observed profiles (Fig. B2). In Fig. B2 the lines represent modeled values, and crosses measured ones. As it can be seen such model may describe majority of the observed profiles, but there is a big difference between widths for the VBLR component estimated using $k_{20,30}$ vs. k_{10} . Also, in this case we obtain that larger fraction of observed AGN has $Q = \text{F}_{\text{ILR}}/\text{F}_{\text{VBLR}} < 1$, i.e. that the VBLR component is dominant in line profiles. Comparing these two models (see Figs. 6 and B2), we found that the two-component model with the disk emission gives more consistent results (Q and i , see Table 1)

In principle for some kind of investigation it is useful (and quite simpler) to use the two-Gaussian fit, but here we aim to investigate possible presence of the disk emission in single-peaked lines, and physically the two-component

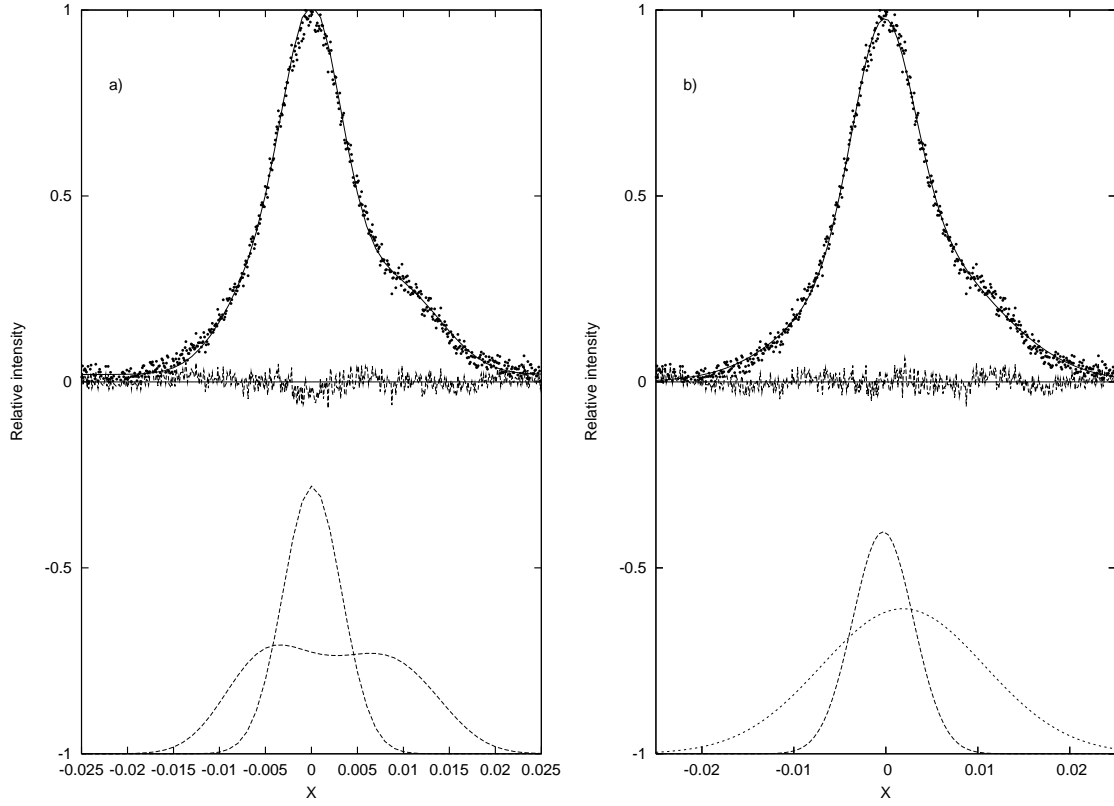


Figure B1. The best fit with two broad Gaussian (left) and with two-component model (right) of 3C273 (see Popović et al. 2004) where one component is assumed to be emitted from the disk (a double peaked component below).

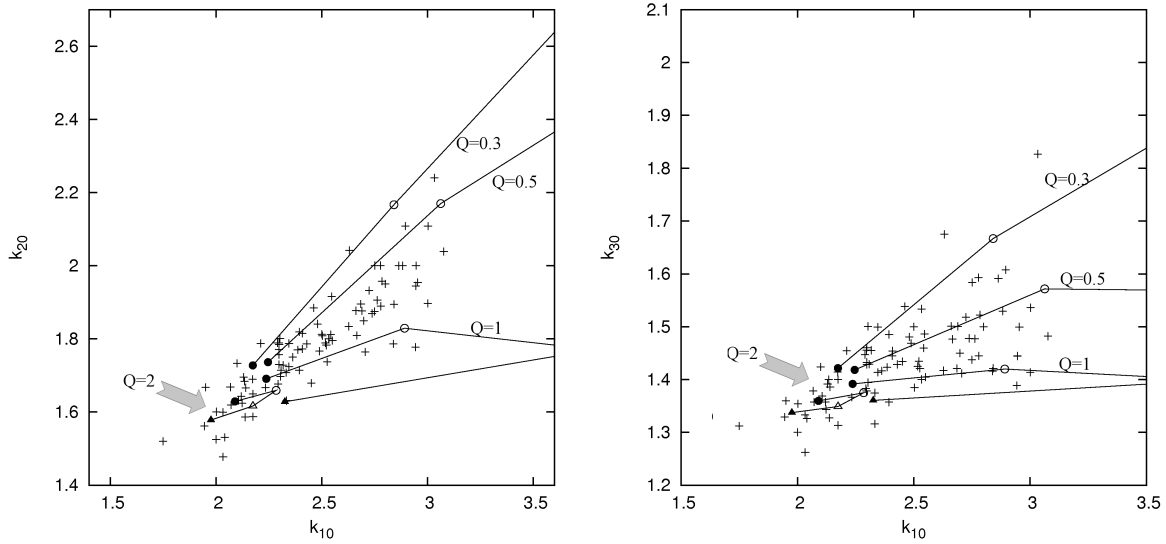


Figure B2. The measured width ratios (crosses) and simulated values (lines) from the two-Gaussian model for the different contribution of the disk emission to the total line flux ($Q = F_{ILR}/F_{VBLR}=0.3, 0.5, 1, \text{ and } 2$). The width of the ILR component is fixed as 1000 km/s, and with the VBLR component is taken as 2000 km/s (full circles), 3000 km/s (open circles), 5000 km/s (open triangles) and 10000 km/s (full triangles).

model with a disk emission seems to better explain the nature of AGN.

This paper has been typeset from a \TeX / \LaTeX file prepared by the author.

